Journal of Applied Physics

RESEARCH ARTICLE | FEBRUARY 23 2024

Fully discrete model of kinetic ion-induced electron emission from metal surfaces

Jorge Fernandez-Coppel ; Richard Wirz; Jaime Marian

J. Appl. Phys. 135, 083301 (2024)
https://doi.org/10.1063/5.0188000

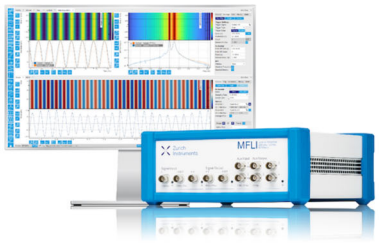

Journal of Applied Physics ARTICLE pubs.aip.org/aip/jap

Fully discrete model of kinetic ion-induced electron emission from metal surfaces

Cite as: J. Appl. Phys. **135**, 083301 (2024); doi: 10.1063/5.0188000
Submitted: 17 November 2023 · Accepted: 1 February 2024 ·
Published Online: 23 February 2024

View Online Export Citation CrossMark

Jorge Fernandez-Coppel,[1] Richard Wirz,[2] and Jaime Marian[1,3,a)]

AFFILIATIONS

[1]Department of Materials Science and Engineering, University of California, Los Angeles, Los Angeles, California 90095, USA
[2]School of Mechanical, Industrial, and Manufacturing Engineering, Oregon State University, Corvallis, Oregon 97331, USA
[3]Department of Mechanical and Aerospace Engineering, University of California, Los Angeles, Los Angeles, California 90095, USA

[a)]**Author to whom correspondence should be addressed:** jmarian@ucla.edu

ABSTRACT

Ion-induced electron emission (IIEE) is an important process whereby ions impinging on a material surface lead to net emission of electrons into the vacuum. While relevant for multiple applications, IIEE is a critical process of electric thruster (ET) operation and testing for space propulsion, and, as such, it must be carefully quantified for safe and reliable ET performance. IIEE is a complex physical phenomenon, which involves a number of ion-material and ion-electron processes, and is a complex function of ion mass, energy, and angle, as well as host material properties, such as mass and electronic structure. In this paper, we develop a discrete model of kinetic IIEE to gain a more accurate picture of the electric thruster chamber and facility material degradation processes. The model is based on three main developments: (i) the use of modern electronic and nuclear stopping databases, (ii) the use of the stopping and range of ions in matter to track all ion and recoil trajectories inside the target material, and (iii) the use of a scattering Monte Carlo approach to track the trajectories of all mobilized electrons from the point of first energy transfer until full thermalization or escape. This represents a substantial advantage in terms of physical accuracy over existing semi-analytical models commonly used to calculate kinetic IIEE. We apply the model to Ar, Kr, and Xe irradiation of W and Fe surfaces and calculate excitation spectra as a function of ion depth, energy, and angle of incidence. We also obtain minimum threshold ion energies for net nonzero yield for each ion species in both Fe and W and calculate full IIEE yields as a function of ion energy and incidence angle. Our results can be used to assess the effect of kinetic electron emission in models of full ET facility testing and operation.

I. INTRODUCTION

Ion irradiation of material surfaces is an important process with applications in medicine,[1,2] dopant implantation,[3–6] space propulsion,[7–9] spectroscopy,[10] and nuclear energy and technology.[11,12] When charged particles collide with solid materials, a number of processes may occur related to the transfer of energy from the incoming particle to the host material. These processes take place until the particles are either absorbed (thermalization), rejected (backscattering, reflection), or transmitted (degradation) through the host metal matrix. While each one of these involves potentially distinct mechanisms, the fundamental process by which charged particles exchange energy with the host material is governed by Coulomb interactions. The ability of a material to decelerate energetic particles traveling within it, or more precisely, the amount of kinetic energy the projectile loses relative to the distance traveled within the material, is referred to as *stopping power*.[13,14] The stopping power is typically expressed in units of electronvolts per angstrom (eV/Å) or Hartree per Bohr radius (E_h/a_0). Crucial parameters for characterizing stopping power include the material's species, phase and microstructure, density, and temperature, as well as projectile type and its kinetic energy or velocity upon impact.

Two regimes are generally considered to define the stopping power in a material. The first is the *electronic stopping* regime, which pertains to high incident particle velocities, where energy losses are primarily due to screened Coulomb interactions between the incoming particles and electrons in the outer shells of the host atoms.[13,15] By contrast, at low velocities, most of the energy is lost through effective interactions with the host ions,[13,16] and, accordingly, this regime is termed the *nuclear stopping* regime. Generally, high-energy irradiation of material surfaces encompasses both regimes, as the projectiles

first lose energy due to electronic stopping and then transition into the nuclear stopping regime once their velocities have been sufficiently reduced. While nuclear stopping can be modeled relatively straightforwardly using classical ion interactions by employing appropriate potentials,[13] modeling electronic stopping is nontrivial due to the complex nature of electron-charged particle interactions.

During electronic stopping, the transfer of energy from the traveling projectile to outer-shell electrons leads to the excitation of these electrons and potential ionization of the host atoms. In most cases, the excited electrons thermalize after losing sufficient energy through elastic and inelastic collisions with the environment.[17,18] However, on occasion, electrons may reach the material surface with sufficient energy to escape into the vacuum, giving rise to net electron emission. When the incident particles are electrons themselves, this process is referred to as *secondary electron emission* (SEE),[19,20] whereas in ion irradiation, the process is known as *ion-induced electron emission* (IIEE).[21] At a minimum, the energy needed by the electrons to escape the surface must be greater than the so-called *work function*, i.e., the electrostatic barrier associated with the existence of a material surface.

In electric thruster devices for space propulsion, ion sputtering and electron emission pose significant challenges to the spacecraft's operational lifetime. Sputtering leads to chamber wall erosion, causing a loss of specific impulse, efficiency, and component damage. Additionally, high secondary electron emission (SEE) and ion-induced electron emission (IIEE) yields can lead to the reversal of the potential sheath that protects the chamber from highly energetic discharges.[22,23] This physical phenomenon can then result in damage to the chamber materials and emission of energetic electrons into the plasma, disrupting thruster operation and resulting in a loss of ionization efficiency. Consequently, the thruster community has shown keen interest in addressing SEE and IIEE issues, leading to the proposal of various methods for electron emission and sputtering mitigation.[24,25] In this context, modeling and simulation can play an important role in accelerating device materials discovery and to define risk mitigation strategies for materials testing and certification. Our group has developed accurate models for SEE in metallic and ceramic material surfaces,[26,27] including morphologically tailored micro-architected materials.[28] In this paper, we turn our attention to IIEE modeling to complement our studies of SEE processes and gain a more complete picture of electric thruster chamber and facility material degradation processes.

IIEE is notoriously challenging to model. In the electron stopping regime, at high ion velocities, ion–electron interactions are generally treated classically. However, except for rare exceptions,[29,30] our models date back several decades ago[31–34] and fail to capture the discrete nature of particle interactions or the complex dependence of the stopping power on incident particle type and material characteristics. At low ion velocities, the vastly different masses of ions and electrons lead to a large disparity in particle velocities, which necessitates a quantum mechanical treatment based on first-principles simulations.[35–37] In the intermediate velocity regime, first-principles simulations are too costly to be practical, while existing continuum models are too approximate. In addition, while data exist at high incident particle velocities (although also decades old in most cases), virtually no experimental data are available for low velocities in metals, making validation challenging in the regime where IIEE takes place during space propulsion.

To bring new computational methods and an improved understanding of charged particle interactions to modeling IIEE, in this paper, we develop a classical discrete ion-induced electron excitation model using energy-dependent stopping power functions. Ion trajectories in a material are simulated using a stochastic binary collision model. During each ion-atom collisional event, the incoming ions lose energy to electronic stopping, exciting a finite number of electrons in accordance with the physical interaction laws of each excitation process in the material. When the excited electrons have an energy larger than the work function, Φ, plus their binding energy to the atom nucleus, E_b (which can range between the Fermi energy, E_F, for core electrons, and zero for conduction electrons), we track their trajectories using previously developed electron scattering Monte Carlo methods until either thermalization or escape. We then tally up the results and calculate IIEE yields as the total number of emitted electrons in relation to each incoming ion. In this work, we consider Xe, Kr, and Ar irradiation of Fe and W metal surfaces. Figure 1 shows a schematic diagram of the processes captured by the model.

In Sec. II, we provide a detailed description of theoretical methods employed and their implementation into numerical simulation techniques, including Appendix A with a validation exercise of the codes developed. In Sec. III, we provide our main results, emphasizing the dependence of the IIEE yields on incoming particle type, particle energy, angle of incidence, and material type. In Sec. IV, we provide a discussion of our findings and their connection with electric thruster technology. We finalize with our most important conclusions in Sec. V.

II. THEORY AND METHODS

In terms of electronic stopping, materials can be broadly categorized as metallic (conductors) or ceramic (insulators). Their respective mechanisms of ion energy loss are:

- In metals, secondary electrons lose energy through interactions with conduction electrons via collective vibrations (known as "polarons"), via core-electron excitation, and with interactions with defects.[38–40] This variety of mechanisms results in relatively large collision cross sections, leading to faster energy loss and subsequent thermalization of secondary electrons before they can escape to the surface. The highly populated conduction band in metals enhances the collision probability with secondary electrons, thereby reducing their chances of escape. Additionally, when impinging ions lose energy to the electron cloud in metals, the greater number of conduction electrons results in a broader energy distribution. This leads to more electrons "stopping" the projectile, which reduces the energy transfer per electron.
- By contrast, in insulators, due to the low number of conduction electrons, internal secondary electrons primarily lose energy through the excitation of valence electrons into the conduction band. This means that only those secondary electrons with kinetic energies above the bandgap can participate in electron–electron collisions. As a result, the energy loss and dissipation of excited secondaries are reduced, leading to increased mean escape depths compared to metals.[41–45]

For insulators, the mean escape depth typically ranges from 10 to 50 nm, whereas for metals, the numbers are 0.5–1.5 nm.[46]

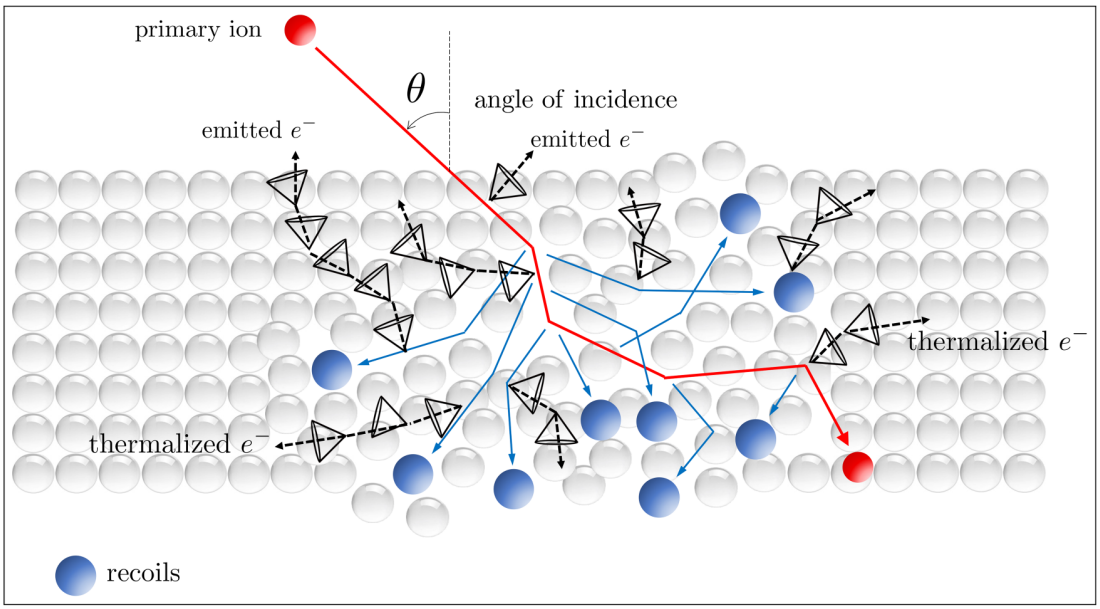

FIG. 1. Schematic diagram showing the different processes captured by the fully discrete model described in this paper. The primary ion (in red) enters the material through its surface and immediately starts exciting conduction electrons due to direct energy transfer. In addition, the primary ion interacts elastically with lattice atoms, creating recoils (host atoms displaced from their lattice positions). These recoils (in blue) can themselves transfer energy and excite electrons deep inside the material. Electrons, whatever their origin, when provided sufficient energy, become mobilized and begin their own scattering processes with other electrons as well as with lattice atoms (represented by open cones). Ultimately, each electron will either thermalize inside the material or escape, giving rise to an emitted electron. Note that even electrons that end up becoming thermalized can conceivably transfer enough energy to other electrons through inelastic collisions, which could conceivably lead to secondary electron emission.

Consequently, insulators exhibit higher yields compared to metals.[26,27,41] Here, we focus on metal surfaces subjected to inert gas ion irradiation (Xe, Ar, Kr). Next, we briefly discuss the existing IIEE models for *kinetic electron emission* (KE), understood as the ejection of electrons from the surface of a material as a result of internal electron stopping processes.[21] Other emission mechanisms exist, such as *potential emission*, where an electron from the solid tunnels into an empty state of the impinging ion (excited neutral) where the released energy is transferred to another electron of the solid, potentially leading to its emission.[34,47–49] This process is also referred to as *Auger* emission, and a brief discussion regarding such process as well as rough estimates for the projectile-target combinations can be found in Sec. IV C. However, in this paper, we will only focus on KE.

A. Analytical IIEE models

One of the first models proposed to characterize KE was that of Beuhler and Friedman[50,51] (B&F). The main assumption in their model is that the electronic stopping power $(dE/dx)_e$ is proportional to the impact velocity of the ion, given by the following equation:

$$\left(\frac{dE}{dx}\right)_e = \frac{N_0 \xi_e}{4\pi\varepsilon_0} \frac{8\pi^2 a_0}{v_0} \frac{Z_1 Z_2 v}{\left(Z_1^{2/3} + Z_2^{2/3}\right)^{3/2}}, \tag{1}$$

where Z_1 and Z_2 are the atomic numbers of the projectile and target atoms, respectively, N_0 is the atomic density of the target, v is the projectile velocity, v_0 is the Bohr velocity, a_0 is the Bohr radius, ξ_e is a dimensionless fitting parameter, and $(4\pi\varepsilon_0)^{-1}$ is a constant factor equal to 9.0×10^9 N m^2 C^{-2}. Likewise, the nuclear stopping power $(dE/dx)_n$ can be calculated as

$$\left(\frac{dE}{dx}\right)_n = \frac{N_0 \pi e a_0}{4\varepsilon_0} \frac{Z_1 Z_2}{\left(Z_1^{2/3} + Z_2^{2/3}\right)^{1/2}} \left(\frac{M_1}{M_1 + M_2}\right), \tag{2}$$

where M_1 and M_2 are the masses of the projectile and target atoms. The total stopping power is obtained as the sum,

$$\left(\frac{dE}{dx}\right)_{\text{tot}} = \left(\frac{dE}{dx}\right)_n + \left(\frac{dE}{dx}\right)_e. \tag{3}$$

The B&F model predicts a constant nuclear stopping power regardless of the impact velocity and is solely a function of the projectile and target properties. In its practical implementation, the B&F model resorts to pre-tabulated velocity–depth (v–x) data in different

materials for calculating the total stopping power,

$$\left(\frac{dE}{dx}\right)_{\text{tot}} = 5.2 \times 10^{-13} \frac{M_1}{x_2 - x_1}\left(v_1^2 - v_2^2\right), \tag{4}$$

where v_1 and v_2 are the velocities at position x_1 and x_2 inside the solid. Combining Eqs. (2), (3), and (4), one can calculate the value of $(dE/dx)_e$. From there, B&F calculates the IIEE yield as

$$\gamma = \frac{P}{E_0}\int_0^{\infty} \exp\left(-\frac{x\cos\theta}{\lambda}\right)\left(\frac{dE}{dx}\right)_e dx, \tag{5}$$

where P/E_0 is the probability that an electron with energy E_0 will escape the surface, x is the depth inside the material, λ is the mean free path of electrons inside the target, and θ is the ion impact angle with respect to the normal of the surface. In effect, Eq. (5) links the total electron yield to the ion velocity v. As such, the B&F model considers IIEE a process driven by ions traveling in straight trajectories through a homogeneous electron gas, with no inelastic collisions or deflections with target atoms. In the high ion-velocity regime, dominated by electron stopping, the B&F model is moderately successful in predicting experimental yields in several materials.[52] However, as the ion slows down, the model approximation of constant nuclear stopping becomes increasingly inaccurate, failing to agree with experiments.[9] It should also be noted that, in general, the mean free path of electrons is energy-dependent at low energies (down to some limit), where energy losses to plasmons become increasingly more important.[53] B&F's model also fails to capture this.

Another limitation of the B&F model is its inability to capture the contribution of recoils to electronic stopping, i.e., the excitation of electrons from displacement collisions between the main projectile and the target atoms. To address this, Schou[33] derived an analytical closed-form solution for the IIEE yield to account for this ionization phenomenon,

$$\gamma = \Lambda\left[\beta_0\left(\frac{dE}{dx}\right)_e + \beta_r \frac{\eta_t(\mu E)}{\mu E}\left(\frac{dE}{dx}\right)_n\right]_{x=0}, \tag{6}$$

where Λ is a material constant, β_r and β_0 are the atomic recoil transport and electronic recoil transport coefficients, respectively, η_t is a 0th-order moment of the energy distribution, and μ is the efficiency of energy transfer between collisions, with $\mu_e E$ being the maximum possible energy transferred. The stopping powers are defined for $x = 0$ (entry point of the material). In Eq. (6), there is now a clear distinction between the contribution from the primary projectile (first term in the r.h.s. of the equation) and recoil cascades (second term). However, even though Schou's model has been utilized broadly to obtain IIEE yields,[54] especially for energy ranges where the contribution of recoils to electron emission cannot be neglected, it relies heavily on empirical constants, which are complicated to obtain. For instance, Λ is difficult to compute analytically and relies on stopping powers for low-energy projectiles with uncertain energy loss functions for calculations above the target's Fermi energy.[54]

B. Semi-discrete model of ion-induced electron emission

To address the issues associated with an incomplete physical description of the electronic and nuclear stopping, the inclusion of recoils, and the empiricism of the B&F and Schou models, here we develop a semi-discrete method of ion-induced electron excitation based on data obtained from the stopping and range of ions in matter (SRIM) calculations.[55] The SRIM code uses highly accurate stopping power tables based on updated experimental data[56] and tracks the trajectories of individual ions inside a material throughout a sequence of collisional events, including those of the recoils displaced from their original locations by direct impact with the primary ion. This information can then be used to track the energy lost by each recoil after each collision to generate $(dE/dx)_e$-vs-E tables for the materials in question. One can then utilize these tables for fast interpolation or to fit the data to generate smooth energy-dependent $(dE/dx)_e$ functions. Figure 2 provides the electronic stopping power predictions using Eqs. (1) and (2), as well as those obtained from SRIM stopping tables, for the energy ranges of interest and various projectile-material combinations. The figure clearly shows that, while the electronic stopping power from the B&F and SRIM models are in reasonably good agreement at high ion energies, the assumption of constant nuclear stopping made in the B&F model becomes increasingly inaccurate at low energies. This may lead to an underestimation of total emission yields, as the extra energy lost to lattice atoms in the B&F model is then unavailable to mobilize internal electrons that may ultimately escape the material. In addition, a higher nuclear stopping power results in shallower penetration of the projectile and, thus, an inaccurate depiction of electron excitation depths.

As an aside, the nuclear and electronic stopping powers from SRIM[57] for moving recoils in W and Fe are shown in Fig. 3. As the figure indicates, the overall electronic stopping power of tungsten recoils is higher than for Fe. This indicates that the amount of energy transmitted from the recoiling atoms to the electron cloud is larger in W, which should in principle result in larger contributions to IIEE from recoils.

Once available, the SRIM functions or tables can be directly used within the B&F model,

$$\gamma_{\text{ion}} = \frac{1}{N}\sum_i \sum_m \frac{P}{E_0}\exp\left(\frac{-x_m\cos\theta}{\lambda}\right)\left(\frac{dE}{dx}\right)_{e,m}, \tag{7}$$

$$\gamma_{\text{recoils}} = \frac{1}{N}\sum_i \sum_j \sum_k \frac{P}{E_0}\exp\left(\frac{-x_k\cos\theta}{\lambda}\right)\left(\frac{dE}{dx}\right)_{e,k}, \tag{8}$$

where the subindices i, m, j, and k refer, respectively, to the number of ions in a simulation, to the number of entries per ion, to the number of recoil cascades produced by each ion, and to the number of recoils in each cascade. N is the total number of ion tracks simulated, With this, the total IIEE is then defined as

$$\gamma_{\text{tot}} = \gamma_{\text{ion}} + \gamma_{\text{recoils}}. \tag{9}$$

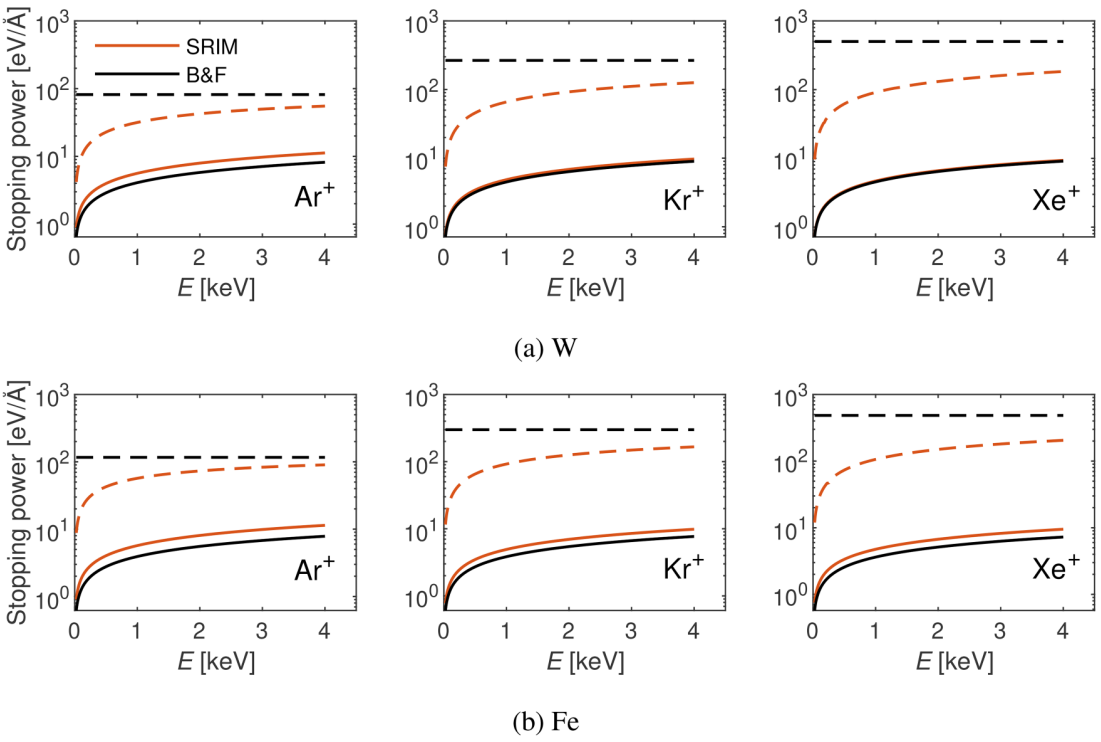

FIG. 2. Stopping power for (a) tungsten and (b) iron obtained from SRIM's libraries (red) as well as Eqs. (1) and (2) (black). Solid lines refer to electronic stopping, and dashed lines refer to nuclear stopping.

1. Electron excitation model for semi-discrete IIEE simulations

A more accurate representation of IIEE can be accomplished if the number of excited electrons in between ion or recoil collisions can be calculated from knowledge of the electronic stopping at each location. For that, first, we make two key approximations:

(1) We assume that $(dE/dx)_e$ decreases linearly with velocity, consistent with other works.[36,58,59] This amounts to assuming that the mean ion collision distance is sufficiently short to allow for a linear discretization of the ion trajectories.
(2) The total energy deposited in the electron cloud between collisions is defined as

$$\frac{dE}{dx} = -ax + b,$$

$$\Delta E = \int_{x_i}^{x_{i+1}} (-ax + b)\, dx,$$

with

$$a = \frac{(dE/dx)_{e,i} - (dE/dx)_{e,i+1}}{(dE/dx)_{e,i+1}},$$

where $b = (dE/dx)_{e,i}$ and x_i is the current collision location.

With this, we can assume that in the appropriate velocity regime, an amount of energy ΔE will be transferred to a homogeneous

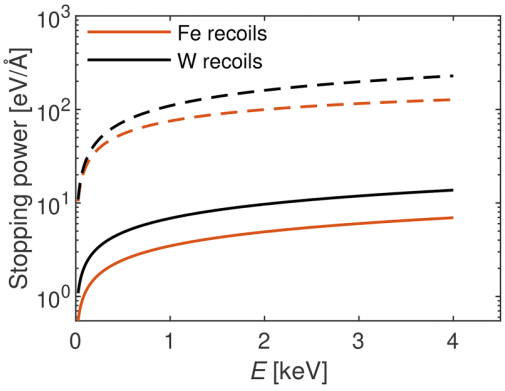

FIG. 3. Stopping power for Fe (red) and W (black) recoils obtained from SRIM's database. Solid lines refer to electronic stopping, and dashed lines refer to nuclear stopping.

electron gas surrounding the ion at all times (this is known to be a satisfactory approximation for metallic materials). This energy is distributed over a number of electrons n_e equal to the electron density times the volume, V, affected by the ion as it moves

$$n_e = V n_0. \tag{10}$$

We can use the Drude model[60,61] to obtain the electron density of a free electron gas as

$$n_0 = \frac{z N_A \rho_m}{m_a}, \tag{11}$$

where N_A is Avogadro's constant, ρ_m is the mass density, m_a is the molar mass, and z is the number of free electrons per atom. For the volume, we use a cylinder with a radius given by the van der Waals radius of the projectile or recoil atom, r_W and a length equal to the intercollision distance $\Delta x = x_{i+1} - x_i$,

$$V = \pi r_W^2 \Delta x. \tag{12}$$

In Eq. (11), z is generally taken as the number of valence electrons. However, here we use a linear relation for z as a function of the incident ion energy justified through validation studies provided in Appendix A. This linear correlation is consistent with the participation of both s and d electrons in the conduction band at finite temperatures in W[40,62] and Fe.[63,64]

The energy ascribed to every electron in V is then

$$E_e = \frac{\Delta E}{n_e}. \tag{13}$$

If $E_e > E_b + \Phi$, an electron is mobilized and assumed to depart the cylindrical volume with a velocity equal to $v_e = \sqrt{2E_e/m_e}$ from a random position within V and a direction sampled from a cosine distribution centered along the cylindrical axis (m_e is the mass of the electrons). The trajectory of these electrons is then tracked using our scattering Monte Carlo (s-MC) techniques[26,27] from their point of mobilization until they either thermalize (i.e., their energy becomes smaller than the work function plus the Fermi energy) or escape the material through the surface. The s-MC code has been specifically designed for metallic materials and accounts for four main scattering processes: elastic scattering, plasmon excitation, inner shell electron ionization, and conduction electron excitation.[26] The values for Φ and E_F used in this work are given in Table I. In this work, we limit the interactions of atoms with electrons to conduction electrons only, as studies have shown that they are primarily the ones that contribute to electronic stopping in metals. For that reason, we take $E_b = 0$ going forward.

TABLE I. Work function and Fermi energies for Fe (values for stainless steel) and W with source indicated in each case.

Material	Φ	E_F	Units
Fe	4.5[65]	11.1[66]	eV
W	4.55[67]	9.6[68]	eV

III. RESULTS

A. Semi-discrete Beuhler-Friedman model

1. Energy deposition and electron excitation profiles

We first examine the depth distributions of the excited electrons as a function of ion type and energy using SRIM-generated stopping powers. All the results shown here are for normal ion incidence. In the original B&F model, the emission probability follows a Gaussian tail that decays exponentially into the material ($x > 0$) from its maximum value at the surface of P/E_0 [see Eq. (5)]. Figure 4 shows the depth profiles obtained using SRIM (Figs. 2 and 3) for all electrons excited by the primary ion and recoils for different target-projectile combinations at 1.6 and 3.2 keV. Visual inspection reveals a maximum inside the material, at a depth that increases with incident ion energy. Note that these results alone signify an improvement over the original B&F model, which could be conceivably augmented by using the profiles given in the figures instead of the fixed exponential decay function. This will be evaluated in Sec. III A 2.

It can be appreciated that the heavier the projectile, the more electron excitation occurs close to the surface. This is consistent with larger collision cross sections and a larger energy fraction transferred to the electrons in the material. Additionally, for the same projectile particle, a higher amount of electrons are excited close to the surface in W relative to Fe. We believe this to be a consequence of the larger angular deflections experienced by the projectile when impacting heavier targets, as discussed in the SRIM documentation.[55]

2. IIEE yields from the improved Beuhler-Friedman model

We now present our results for all the projectile-target combinations of interest to this study using SRIM-generated stopping powers to the standard B&F analytical model. In effect, this implies replacing the integrand in Eq. (5) with the discrete sum shown in Eq. (3) that incorporates SRIM-generated electronic stopping powers. Figure 5 shows IIEE yields from the original B&F, and the SRIM-improved B&F models, separating the contributions to electron excitation from ions and recoils. IIEE yields increase monotonically with ion energy and range between 0.2 and 1.0 in W for ion energies in the 0.5-to-4.0-keV interval.

The results unequivocally show that the original B&F model underestimates the total ion-induced electron emission yields. In W, there is a factor of three difference between the total yields with the improved electronic stopping data and the original model. In Fe, the difference is approximately a factor of two. Another difference worth remarking is the relative importance of ion vs recoil induced electron yields. Recoils appear to be more important in W compared to Fe. Going back to Fig. 4, the electronic stopping power for tungsten on tungsten is approximately twice that of Fe on Fe. This, together with the fact that the interactions between recoils and bulk electrons occur closer to the surface for tungsten, results in substantially larger recoil contributions to IIEE in the heavier material. In terms of the effect of the projectile species on

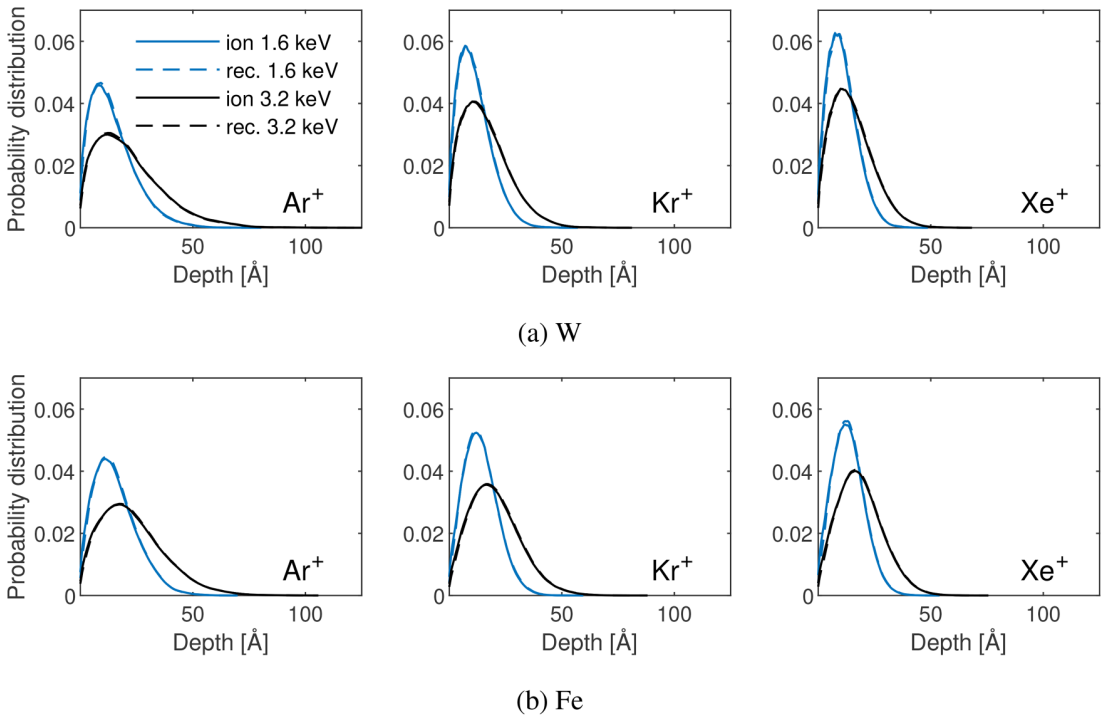

FIG. 4. Depth excitation profiles for (a) tungsten and (b) iron.

IIEE, an inverse proportionality between the size of the impinging ion and the predicted yields is observed. This is consistent with the results shown in Fig. 2, which shows that the electronic stopping power decreases with increasing projectile size.

B. Fully discrete IIEE model

Next, we provide results for the fully discrete model, consisting of an ion-target interaction module, driven by SRIM simulations, and an electron transport module driven by a scattering Monte Carlo model.

1. Energy deposition and electron excitation profiles

We start by calculating electron excitation energy spectra. Figure 6 shows results for Ar, Kr, and Xe ions with an incident energy of 2.8 keV and normal incidence. The figure illustrates two key aspects: the excitation energy distribution resulting from the primary ion and recoils (where recoil energy distributions are the same for all ion species) and the depth distribution of the excited electrons, representing the histogram of the locations of ion or recoil-induced electron excitations. As the results show, the range of energies of the excited electrons is rather low, $<$7.0 eV for primary excitation in W and $<$6.0 eV in Fe. Recoil excitation results in a majority of electrons with energies well below the work function, although the tail of the distributions spans to higher energies of about $<$ 7.0 eV in W and $<$2.0 eV in Fe. Also shown are the depth distributions, both for primary ions (solid lines) and recoils (dashed), which resemble skewed Gaussians (Maxwellian) with maxima around 20 Å. These depth distributions mimic those of the ions themselves given the direct connection between ion trajectories and electron excitations.

The energy spectra of electrons excited by the primary ions deserve further commentary. In all cases, two clearly defined peaks can be appreciated, one at very low energies and the other toward the tail of the distribution. The first one is a consequence of direct interactions between the incoming ion and the electron cloud near the surface of the target material, before the first collision with a target atom. This peak is commonly seen in experimental measurements and is traditionally attributed to Auger emission (potential IIEE).[69–71] By contrast, the second peak arises from ions coming to a complete stop, after their energy drops below the threshold displacement energy to mobilize more recoils (40 and 25 eV, respectively, for W and Fe). Another shared characteristic across the different target materials is the shift of the second peak to lower energies as the atomic number Z increases for the projectile ions. This shift is likely due to the smaller projectiles having a higher electronic stopping power, as illustrated in Fig. 2, combined with their lower van der Waals radii. This results in a smaller, yet more intense, interaction volume and subsequently more energy distributed to fewer electrons. Along similar lines, Figs. 7 and 8 show excitation energy spectra and excitation electron depth distributions for three angles of incidence ($\theta = 15°$, 45°, and 75°) in W and Fe,

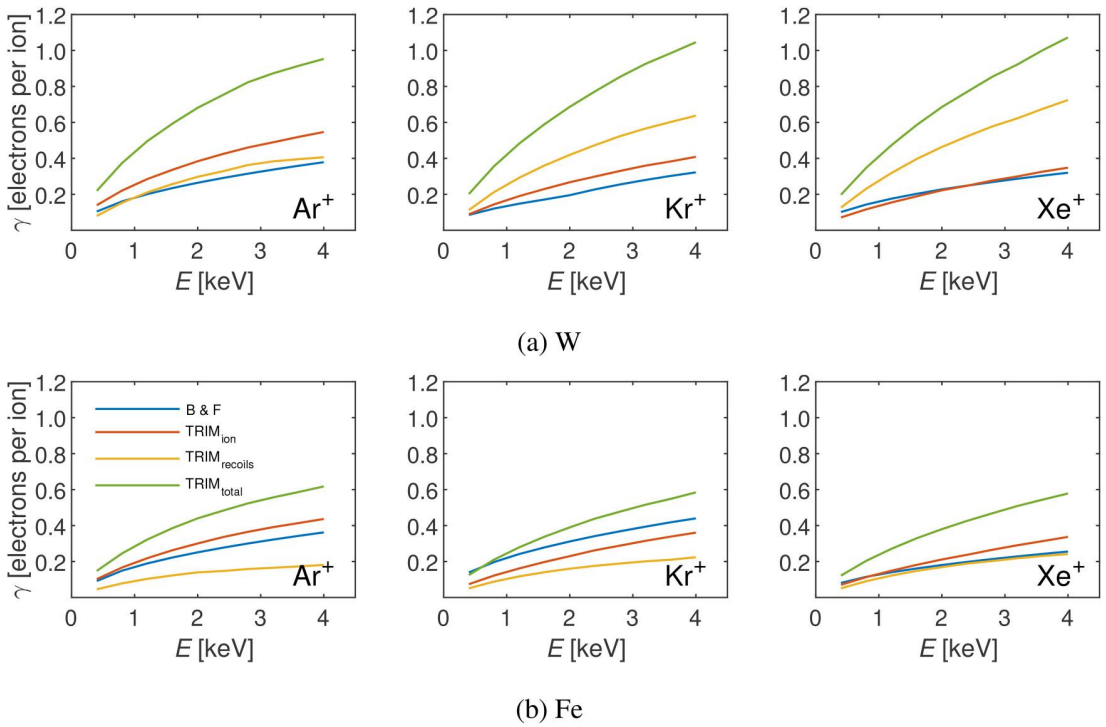

FIG. 5. IIEE from B&F original and improved models for (a) tungsten and (b) iron.

respectively. The distributions are obtained considering ions with an incident energy of 4.0 keV. Only electrons with energies larger than $E > \Phi + E_b$ (work function plus difference between Fermi level and initial energy level of excited electron) are shown.

The results for W show that the far energy peak (at ≈6.0 eV) intensifies as the incidence angle increases for all ion types (although more strongly for Kr). This is due to the shallower penetration of ions as the angle of incidence increases, which excites more electrons near the surface. This is confirmed by the depth distributions, which show a clear strengthening of the excitation peaks near the surface as θ increases. When the ion penetrates the target with a high angle relative to the normal of the surface, there is an increased probability that it will backscatter or stay near the surface region as given by elastic scattering theory. This results in the step-like behavior observed in the depth profiles given in Figs. 7 and 8. The results for Fe in Fig. 8 are qualitatively equivalent to those of W. However, the fraction of electrons with energies above the emission threshold are significantly lower in Fe compared to W (in fact, no excited electrons with $E > \Phi + E_b$ exist for Xe irradiation or for recoil excitations).

Our final piece of analysis is the study of the scattering angle of the excited electrons at the surface. The scattering angle distribution function used in this work for local collisions is a cosine distribution centered at zero degrees, which is taken as the direction of the incoming ion before the collision. However, because recoils are effectively displaced in random directions after colliding with the primary ions, the precise scattering directions of the excited electrons are not obvious *a priori*. Figure 9 shows the scattering angular distributions at increasing ion incidence angles for surface electrons excited at a maximum depth of 2 Å. In the plots, 0° and ±180° correspond to directions into and away from the surface, respectively. The results show that the most probable scattering directions (mode of the distributions) correlate with the angle of incidence. However, it is interesting to see how for W, which is highly refractive, there is also a considerable amount of surface electrons excited toward the vacuum, particularly for the combinations that show the highest amount of backscattering. This could signify a relation between backscattering coefficients and IIEE at the low-energy regime and will be discussed along our IIEE results.

2. IIEE yields from the fully discrete model

After discussing the different aspects that could have an effect on emission yields, we present our results for IIEE of the different projectile-material combinations utilizing the full discrete model. An intermediate validation/parameterization study in conditions conducive to kinetic-only electron emission is provided in Appendix A, which adds confidence to our approach. Figure 10 shows three-dimensional meshes with IIEE yields as a function of incident energy E and angle θ in tungsten. The figures contain results for each incident ion type and show the partial contributions to the total IIEE yield due to recoils, the primary ion, and the total yield.

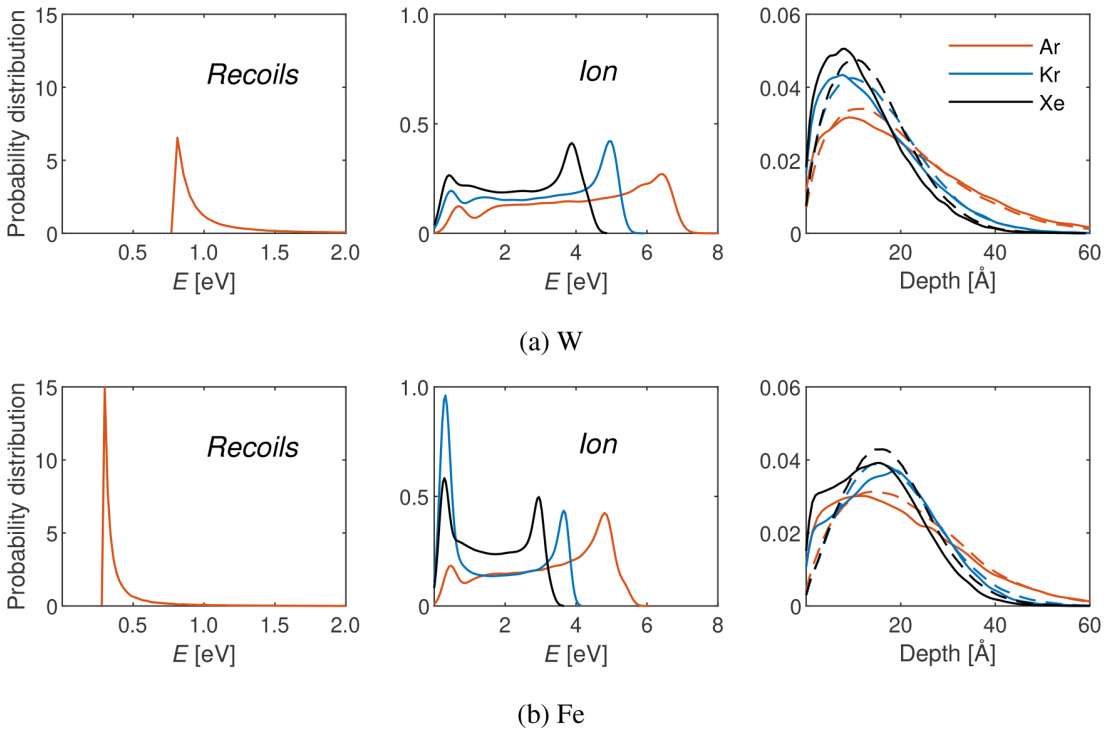

FIG. 6. Electron excitation profiles for 2.8-keV noble gas irradiation with $\theta = 0$ for (a) tungsten and (b) Fe. Dashed lines refer to recoils and solid ones to primary ions.

The first observation is the existence of a threshold incident energy for kinetic IIEE from the primary ion, which is seen to scale with ion mass and take values of, approximately, 1.6, 2.8, and 4.0 keV for Ar, Kr, and Xe, respectively. This threshold energy displays a weak dependence with the angle of incidence. Second, when emission from the primary ion starts, its contribution to IIEE clearly dominates over the recoil contribution. However, consistent with the results shown in Fig. 5, the recoil contribution is not zero, and itself requires threshold ion energies of 2.8 keV for Ar, 2.4 keV, for Kr and 1.6 keV for Xe, inversely scaling with mass in opposition to emission thresholds from the primary projectile. In fact, for the energy ranges of this study, recoils are responsible for the entirety of emission in Xe → W impacts. The total yields also are seen to scale with ion mass ($\gamma_{Ar} > \gamma_{Kr} > \gamma_{Xe}$) and increase monotonically as a function of incident energy and angle. For Ar, they reach values of ≈2.5−−5 for an incident ion energy of 4 keV. Regarding the dependence of the total IIEE yields on incident energy, our results indicate a logarithmic or quasi-logarithmic dependence, in general agreement with published ion irradiation studies in W.[54,72,73] The angular dependence displays the classical Yamamura-type scaling,[21,74] with a minimum at normal incidence and a peak at 75°.

The companion results for Kr, Ar, and Xe ion impingement on Fe surfaces are shown in Fig. 11. As anticipated from the results in Fig. 8, Fe experiences much lower IIEE yields compared to W. Indeed, the threshold ion energies for nonzero emission can be extracted from Fig. 11 with values of ≈7.0, 16.0, and 20.0 keV for Ar, Kr, and Xe ion bombardment. In addition, the contribution of recoils to IIEE in this case is virtually zero, such that kinetic emission in Fe can be described as a function of solely the primary projectile. Once again, emission yields increase with decreasing Z, with Ar exhibiting the highest yields followed by Kr and then Xe. In this case, however, the dependence of the yields on incident energy is linear or quasilinear when emission commences, also in agreement with past studies in Fe or stainless steel.[54,75]

Finally, we have calculated the energy spectra of emitted electrons, i.e., energy distributions of secondary electrons, E_{SE}, as if they were measured at a detector in the vacuum. Results for three above-threshold incoming ion energies are shown for both W and Fe in Fig. 12. In all cases, the spectra resemble Thompson energy distributions[76,77] with peaks at very low energies (<0.1 eV in some cases). While in W, the distributions appear to be confined to the same narrow energy range, between zero and 0.2 eV, regardless of ion impact energy, in Fe, longer tails are observed to correlate directly with ion impact energy and inversely with ion mass. In addition, the distributions are consistent with the energy spectra observed in Fig. 7. In the spirit of our model, the energies of the emitted electrons are solely a function of the energy gain from screened Coulomb interactions with the projectile. We should mention that the tails of the distributions for Xe impacts on W at 4 keV are substantially longer than for Kr, creating an exception to this general trend. However, note that this phenomenon may be related to the nature of electron excitations, whereas Xe emission is only a product of recoils.

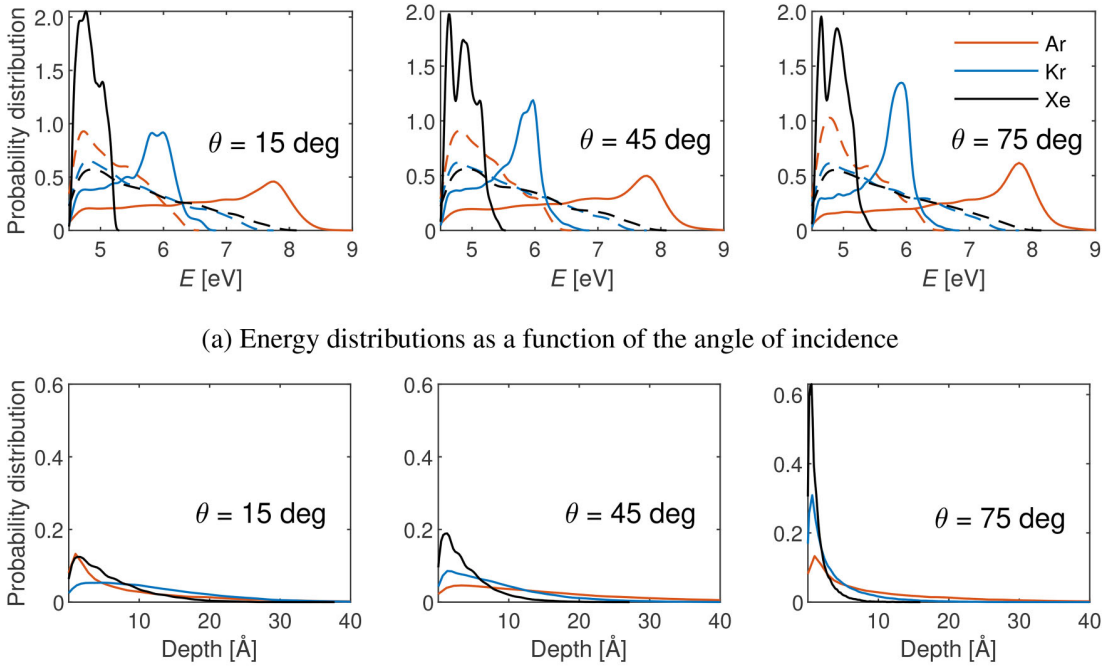

FIG. 7. Excitation profiles of electrons with $E > \Phi + E_b$ for 4-keV noble gas ions collisions with a W target. (a) Energy spectra of the excited electrons. Solid lines refer to the primary ions, while dashed lines indicate the recoil contribution. (b) Depth distributions. (a) Energy distributions as a function of the angle of incidence. (b) Depth distributions as a function of the angle of incidence.

IV. DISCUSSION

A. Motivation for the present model

B&F's[50] and Schou's[33] models have been the reference approaches to calculate kinetic IIEE from metal surfaces since the early 1980s. Both methods are semiempirical continuum models that do not take into account ion–atom or ion–electron collisions explicitly. B&F's model has proven to be accurate in the high velocity regime ($\gtrsim 4 \times 10^7$ cm s^{-1}), when atomic collisions do not take place close to the surface and ion-material interactions are dominated by electron stopping. In this regime, electron excitation is primarily a function of the ion energy and not the projectile species. However, at lower impact energies, as more energy is exchanged with recoils through nuclear stopping, B&F's model becomes too simplistic and is only able to capture the excitation produced by the primary ion. Even then, as shown in Fig. 5, by assuming a velocity-independent nuclear stopping function (see Fig. 2), the B&F model underpredicts the total IIEE yield in the entire energy range. Indeed, our results show that recoils play a major role in IIEE when electronic stopping dominates (e.g., Fig. 3) or when electron excitation takes place at shallow depths leading to superficial depth profiles (Fig. 4). In the recoil-dominated regime, the specific nature of the ion species can no longer be neglected and B&F's model fails to accurately capture IIEE yields.

Schou's model was originally designed to partially address these shortcomings but it does so by assuming a mostly arbitrary partition of the total ion energy into primary and recoil electron excitation contributions. In addition, in Schou's model, the energy going to recoils is distributed uniformly along the ion track, whereas ion trajectories in solids at low energies are characterized by frequent deflections of discrete nature, i.e., they deposit energy in highly nonuniform way. Addressing these limitations through a fully discrete model is the main objective in this paper. We accomplish this by improving the physical fidelity of the model in three main aspects relating to ion–ion and ion–electron interactions,

1. Our first improvement is related to the use of accurate, energy-dependent nuclear and electronic stopping functions, available through the SRIM code distribution.[55] These functions are implemented as lookup tables for fast evaluation, and give the model the precise amount of energy transferred to recoils and electrons by the primary ion. In our case, these include stopping power values of Kr, Ar, and Xe in W and Fe.
2. Recoils are then separately tracked inside the material, each transferring energy to the electron cloud as well. For our calculations, this requires stopping power tables for Fe in Fe and W in W.

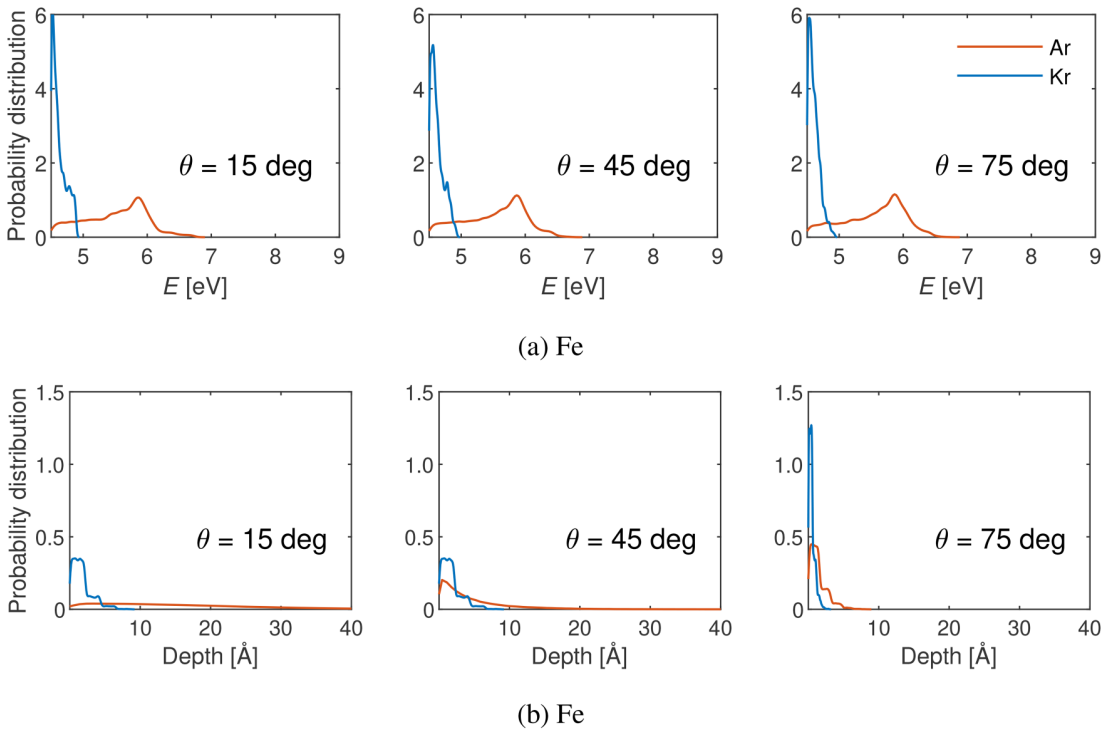

FIG. 8. Excitation profiles of electrons with $E > \Phi + E_b$ for 4-keV noble gas ions collisions with a Fe target. (a) Energy spectra of the excited electrons. Solid lines refer to the primary ions, while dashed lines indicate the recoil contribution. (b) Depth distributions. (a) Fe, (b) Fe.

3. Further, we track all electrons, regardless of whether created by the primary ion or by the recoils, from the point of excitation to the point of thermalization or escape. This is done using a scattering Monte Carlo approach specifically developed for electron transport in metals.[27]

This represents a substantial improvement over the classical analytical approaches. As we will discuss next, our model indeed suggests that IIEE is extremely sensitive to many physical parameters not captured in the earlier semiempirical models.

B. Discussion of main results

Here, we have focused on metallic systems where the general electron gas theory for electron excitation can be applied. Due to their technological importance, in this paper, we have considered W and Fe. These systems, however, are very different in terms of electronic structure, which is reflected unambiguously in their total IIEE yields (Figs. 10 and 11). To first order, the much larger yields in W compared to Fe are likely a result of the much higher electron density of Fe, which in the electron gas approximation implies distributing the incoming ion energy among more electrons, resulting in excitation events. This phenomenon is captured in the electron energy distribution plots given in Figs. 6–8, where it is clear that the electrons excited in W have higher energies than those in Fe. Additionally, the electron density of the host material increases the scattering probability of the excited electrons with other electrons in the conduction band. This results in an increased energy loss from inelastic collisions and subsequently a higher probability of thermalization before reaching the surface. Another important result worth mentioning derived from the IIEE yield distributions is the existence of an energy threshold for nonzero IIEE. This threshold is a complex function of the incident ion properties (mass, energy, angle of incidence) and the host material (mass and electronic structure) and cannot be calculated or inferred accurately using B&F's or Schou's models. Incidentally, capturing this threshold is also one of the main differences between using the semi-discrete (which does not capture it) and the fully discrete approaches (which does).

Another factor that seems to weigh heavily in the IIEE yields is the scattering angle of the electrons close to the surface. As illustrated in Fig. 9, there are cases (as in Ar → W) with a substantial probability of energetic surface electrons scattering toward the vacuum. This is likely due to backscatterers, i.e., ions deflected toward the surface. These backscatters are known to be important contributors to electron emission, especially for low incident ion energies,[21] as electrons excited near the surface by a backscattered ion have a high probability of escape. Consequently, as the angle of incidence deviates from normal incidence, the probability of backscattering increases, which is seen as a shift in the scattering angle peaks and the change in depth distributions in Figs. 7 and 8.

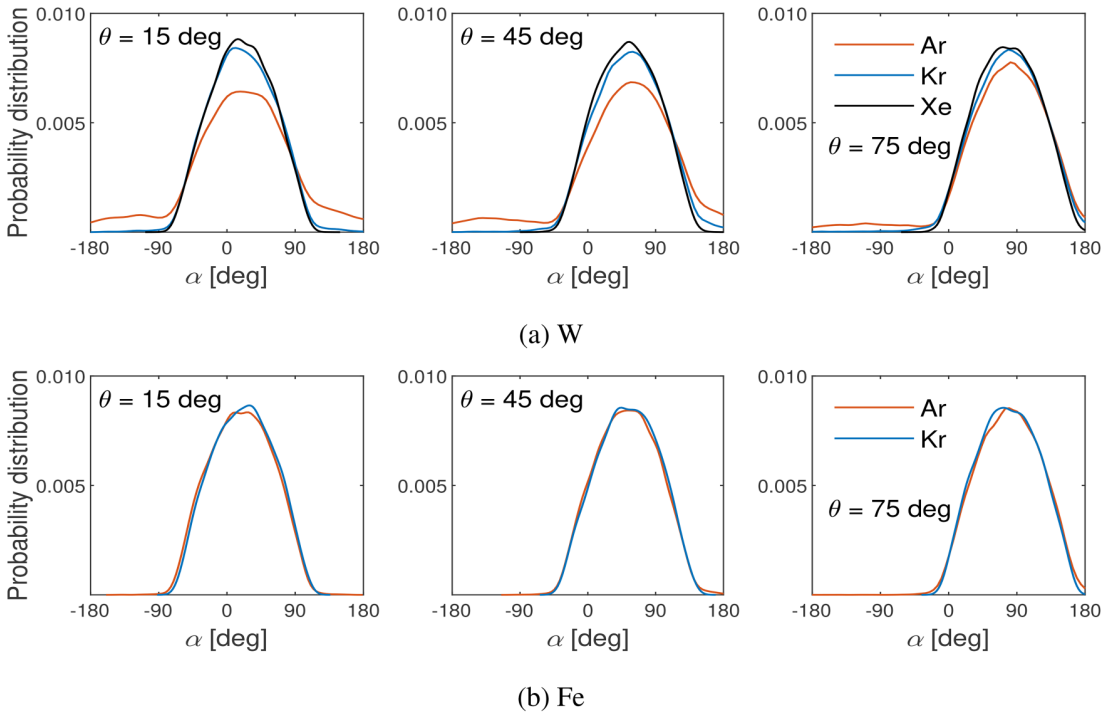

FIG. 9. Scattering profiles of electrons with $E > \Phi + E_b$ excited at depths of x < 2 Å for 4-keV noble gas ion collisions with (a) W target, (b) Fe target. (a) W, (b) Fe.

Regarding recoils, IIEE seems to be mainly due to direct energy transfer from the projectile to the material electrons (and, in fact, our model predicts no electron emission in Fe due to recoils in the energy range explored in this work). However, the consideration of recoils through nuclear stopping is an absolutely essential part of the models, even if recoils themselves do not contribute directly to IIEE, as it dictates the correct amount of energy available for electron excitation by the primary ion. Regardless, there are cases where recoils substantially contribute to IIEE, such as in Xe → W, and, in fact, dominate emission at low energies. Such contributions appear to be substantial in combinations with high nuclear stopping powers with shallow penetration profiles (Figs. 2 and 3), or in other words, for heavy projectiles impacting on dense, heavy targets with low atomic densities.

In terms of using our results in the context of full facility modeling for experimental testing of electric space thrusters, we can conclude that kinetic emission from stainless steel (a common structural material used in test facilities for piping, vacuum vessels, etc.) is negligible and should not be a matter of concern for facility operation. Also, when making design decisions for future EP applications where secondary emission might be of concern, whenever metals are part of the design, we recommend utilizing those with high atomic densities and low backscattering coefficients in order to increase energy dissipation and reduce emission probability. We understand that there is a trade-off between sputtering and IIEE, where highly refractory metals might perform better in terms of mass erosion, but our results indicate that there might be a non-negligible emission probability for the propellant gases utilized in EP when impacting high-Z metal surfaces. This could lead to the reversal of the plasma sheath and the discharge of highly energetic electrons into the wall that could damage the plasma chamber.

C. Limitations of the present model and future work

The present model predicts kinetic IIEE and does not yet account for other emission mechanisms such as potential emission through Auger neutralization, or thermionic emission. Even as it relates to kinetic emission, our model has been specifically developed for metallic surfaces, to which the uniform electron gas approximation can be applied, simplifying the theoretical and numerical treatment of electronic stopping energy transfer and electron scattering processes. Current work by the authors is aimed both at developing an IIEE model for potential emission and to extend the present kinetic model to covalent materials, such as graphite or insulators. For reference, a quantitative estimation of the yields due to potential emission is provided in Appendix B.

Another point worth discussing is the use of ideal surfaces in the model (perfectly flat and non-degradable), whereas it is well known that surface asperities and morphological evolution during ion irradiation have a direct impact on the measured yields. For example, several studies have found a link between surface preparation prior to implantation and the measured ion-induced electron

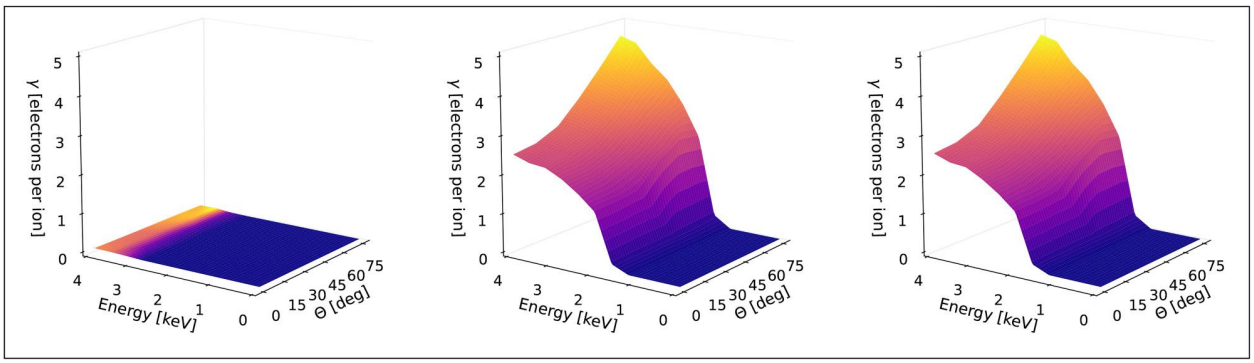

(a) Ar→W

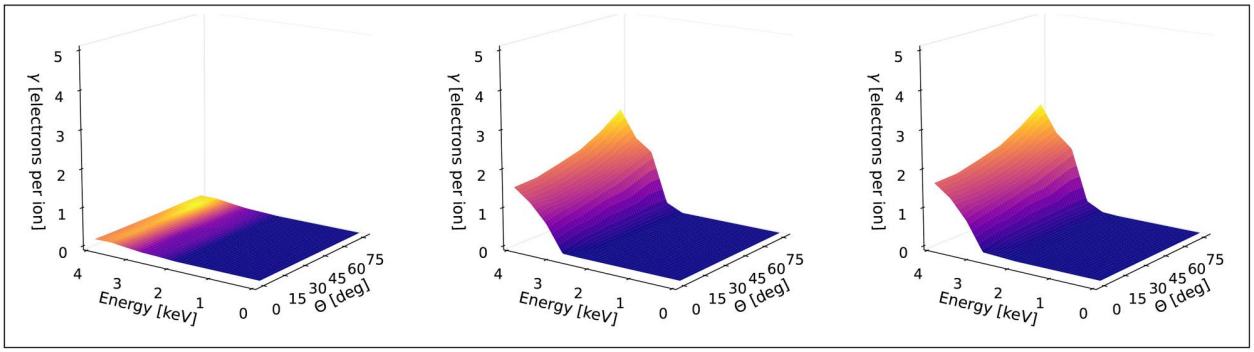

(b) Kr→W

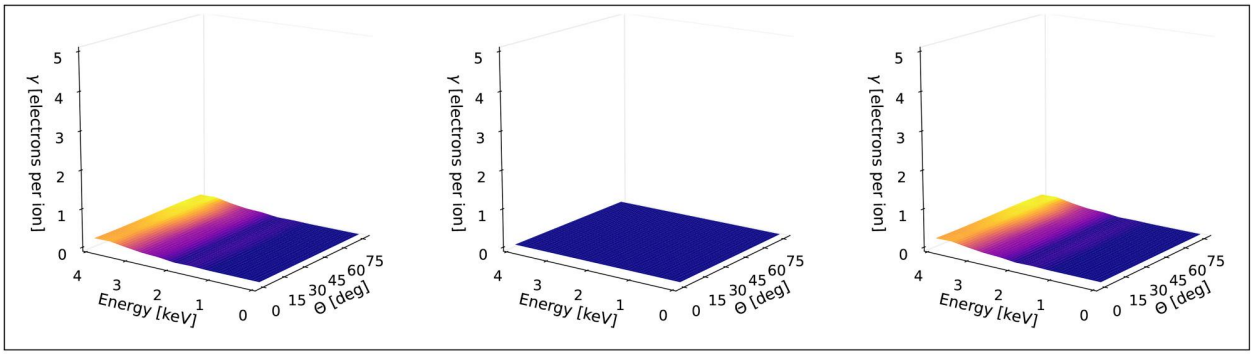

(c) Xe→W

FIG. 10. Kinetic IIEE yields for W utilizing the fully discrete model. From top to bottom: Ar, Kr, and Xe ions. From left to right: recoil contribution, primary contribution, total IIEE. (a) Ar → W, (b) Kr → W, (c) Xe → W.

emission yields.[78] Hasselkamp *et al.*[73] measured IIEE yields during Ar ion irradiation of W surfaces immediately after several hours of ion etching with Ar^+ impacting at 300 keV. These authors report that electron yields were substantially higher at the beginning of ion bombardment, gradually moderating to lower values at steady state. They attribute these changes in total yield to the formation of an oxide layer on the surface. However, other studies have found that ion etching for long periods of time produces several

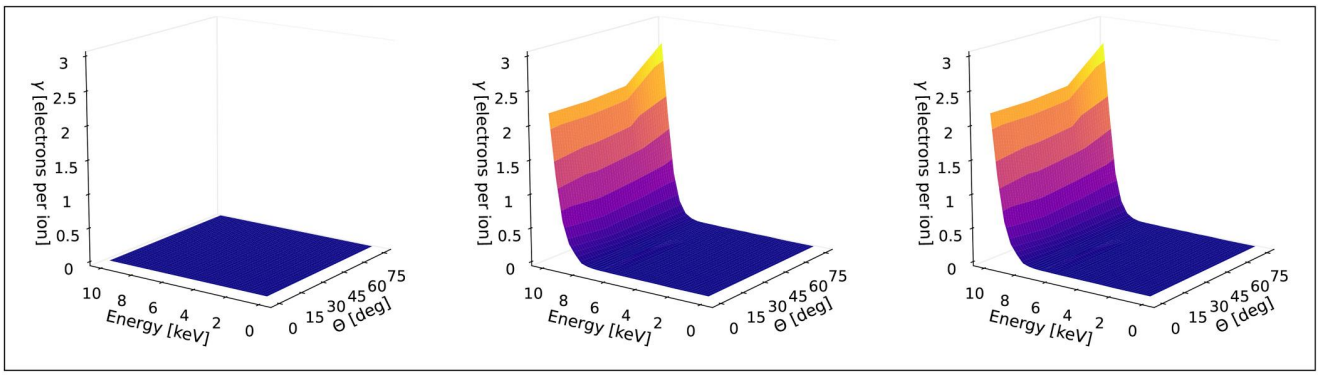

(a) Ar→Fe

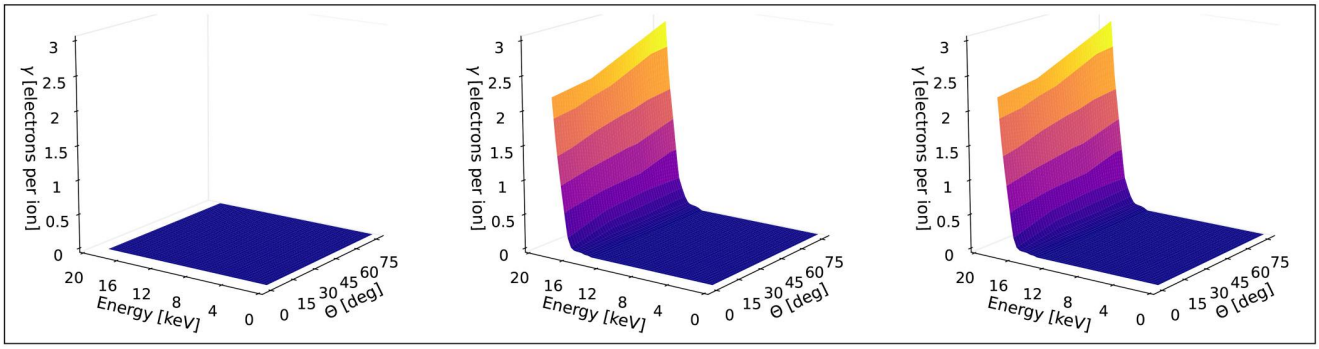

(b) Kr→Fe

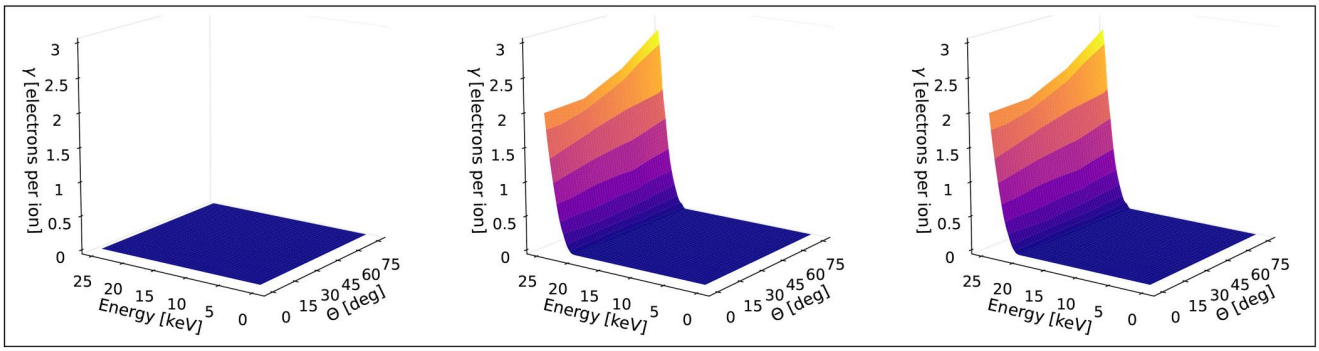

(c) Xe→Fe

FIG. 11. Kinetic IIEE yields for Fe utilizing the fully discrete model. From top to bottom: Ar, Kr, and Xe ions. From left to right: recoil contribution, primary contribution, total IIEE. (a) Ar → Fe, (b) Kr → Fe, (c) Xe → Fe.

undesirable effects on the surface of the metal that could have a non-negligible effect on IIEE.[79–82] Other studies, such as that by Hugonnaud *et al.*,[83] obtained their emission results from the interaction between the plume of an electric thruster[84,85] and the testing facility walls, as an average over 800 data samples acquired over 25 min under much lower ion beam currents and irradiation doses than. Hasselkamp *et al.*[73] This proves that a link exists between the nature of the irradiation source and the microstructural evolution

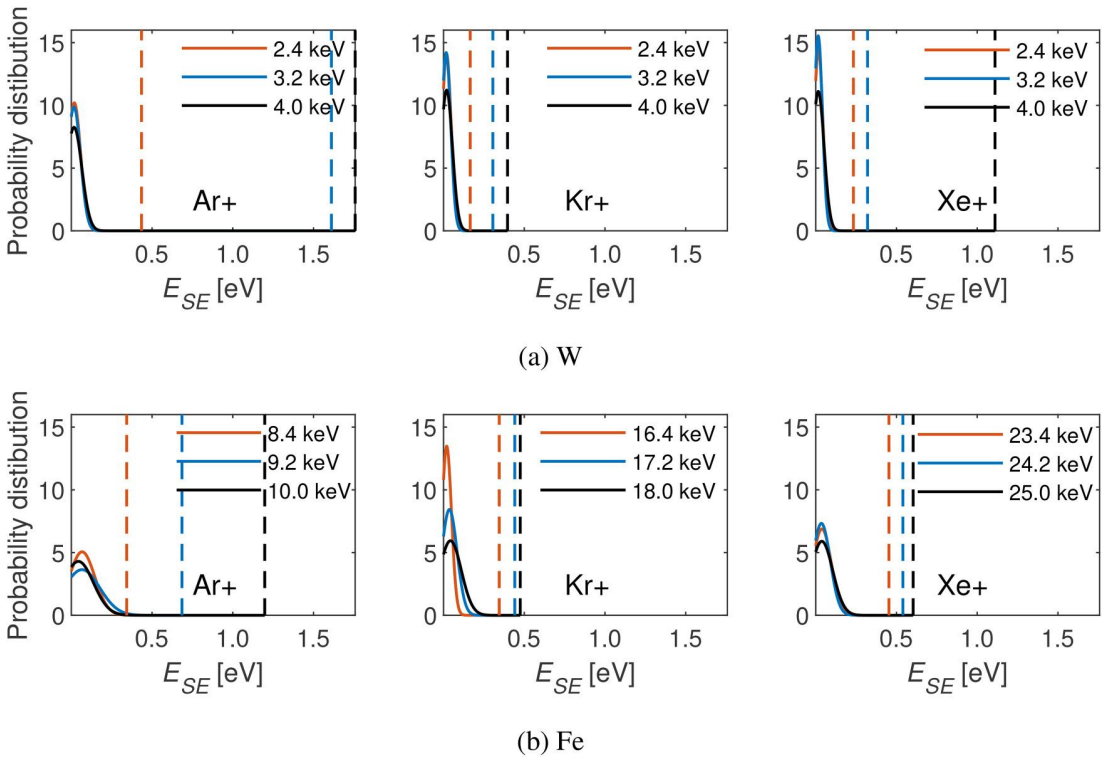

FIG. 12. Emitted electron energy profiles (measured in the vacuum) for (a) tungsten and (b) iron. Dashed lines mark the most energetic emitted electron for each impact energy recorded. (a) W, (b) Fe.

of the material being bombarded, especially close to the surface, resulting in different emission yields. None of these effects are captured in our model, which assumes that the surface is ideally flat and does not vary with time, dose, dose rate, or is subjected to environmental effects.

Finally, despite representing an improvement over current analytical or semi-empirical models, our approach still lacks aspects related to the electronic structure and crystallography of the host materials. For example, while the classical electron gas model (e.g., the Drude model) is appropriate for metals in general, systems such as W possess a complex electronic band structure that makes electrons in different energy bands (orbitals) react different to interactions with external ions. In addition, our model contains no notion of crystallography (in the spirit of the SRIM code, which is based on the binary-collision approximation), whereas it is known that electron transport along high-index directions (i.e., with high atomic packing) has significantly lower mean free paths than along low-index orientations (higher vs lower scattering cross sections).[36,86] This could be an important effect to capture when considering single crystal metallic materials with specific surface orientations at low temperatures. At high temperatures, crystallographic effects are mitigated by thermal fluctuations, which "blur" the atomic lattice structure to excited electrons.

V. CONCLUDING REMARKS

We finish the paper with our most important conclusions.

- We have developed a fully discrete simulator of kinetic ion-induced electron emission from metal surfaces. The model supersedes commonly used semi-analytical models that fail to correctly capture the transfer of energy from the incident ion to host material recoils and electrons.
- The discrete model is based on three theoretical improvements: (i) it uses the latest energy-dependent electronic and nuclear stopping databases to accurately capture ion–recoil and recoil–recoil interactions; (ii) it uses the classical electron gas model to calculate the energies of the excited electrons; and (iii) it uses a scattering Monte Carlo model to track all excited electron trajectories.
- Model predictions were compared to high (In → W, In → Fe) and very high-energy (Ar → W) ion impact data with good agreement achieved in both cases.
- We have compared calculations from the classical semi-analytical models with our improved approach, and find that the classical models underpredict IIEE at all incident energies in the cases of Ar, Kr, and Xe bombardment of W and Fe surfaces.

- We have obtained excitation energy distributions as a function of depth for several incident ion energies and angles.
- We have calculated IIEE yields as a function of incident ion energy and angle in W and Fe surfaces. We find that both materials display clear incident energy thresholds for the onset of nonzero IIEE, with those of Fe about twice as high as those of W. Further, we find that electron emission from noble gas ion bombardment is significantly larger than that of Fe.

ACKNOWLEDGMENTS

This work was partially supported by NASA through the Joint Advanced Propulsion Institute, a NASA Space Technology Research Institute (Grant No. 80NSSC21 K1118).

AUTHOR DECLARATIONS

Conflict of Interest

The authors have no conflicts to disclose.

Author Contributions

Jorge Fernandez-Coppel: Conceptualization (equal); Formal analysis (lead); Investigation (lead); Methodology (lead); Software (lead); Validation (lead); Visualization (lead); Writing – original draft (lead). **Richard Wirz:** Conceptualization (supporting); Funding acquisition (supporting); Writing – review & editing (supporting). **Jaime Marian:** Conceptualization (equal); Formal analysis (supporting); Funding acquisition (lead); Investigation (supporting); Methodology (supporting); Supervision (lead); Visualization (supporting); Writing – review & editing (lead).

DATA AVAILABILITY

The data that support the findings of this study are available from the corresponding author upon reasonable request.

APPENDIX A: VALIDATION AND FITTING OF THE KINETIC IIEE MODEL

Validation and parameterization of our model using experimental data can be challenging due to the limited availability of recent studies on IIEE for specific projectile-target combinations in the low-energy regime. Nevertheless, our model's validity extends, in principle, to kinetic electron emission from any metal surface when impacted by ions of any type. By modifying the inputs of our approach, we can obtain relevant results for a variety of cases.

Here, we compare our model predictions with IIEE yield measurements in W and Fe. First, we consider a recent study performed by Hugonnaud *et al.*[83] of In → W and In → Fe experiments in the 3–8-keV ion energy range. At these incident energies, IIEE is dominated by kinetic emission and, thus, our model is directly applicable without any additional modifications. For this comparison, we use $E_b = 0$ based on the assumption that only electrons in the conduction band participate in stopping at these energies. In our analysis, we treat the variable z in Eq. (11) as an adjustable parameter of the model, allowing it to depend linearly on incident energy to

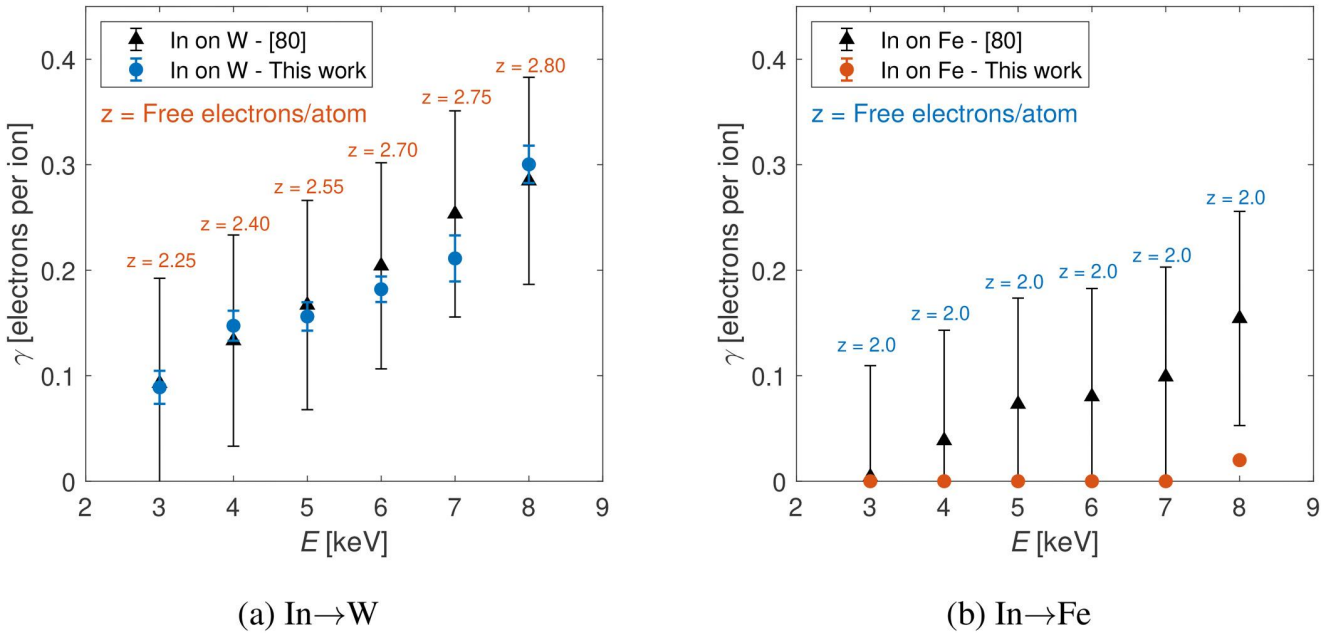

FIG. 13. Comparison between the model predictions and the experimental data by Hugonnaud *et al.*[83] using a linear dependence of z with ion energy. The error bars represent the standard deviation of the values obtained from ten independent simulations using the model presented here. (a) In → W, (b) In → Fe.

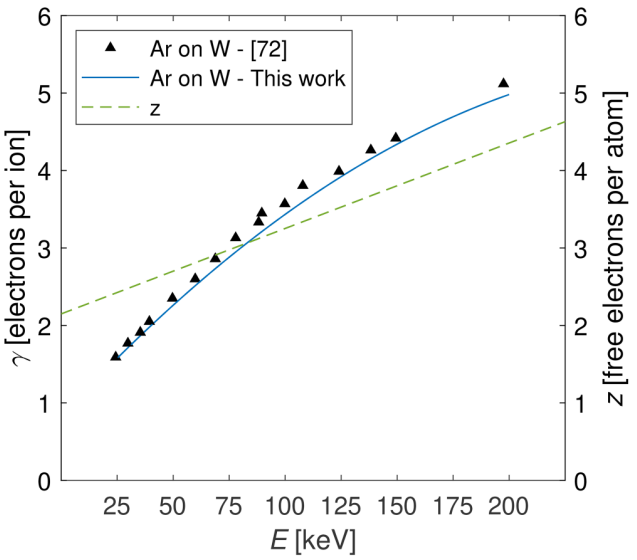

(a) Ar→W

FIG. 14. Comparison between the model predictions and the experimental data by Hasselkamp *et al.*[73] using a linear dependence of z with ion energy. (a) Ar → W.

best match the experimental data. This is consistent with studies of the electronic band structure of metals that have shown that the number of free electrons per atom increases linearly with the electronic temperature.[87,88] Here, we assume a direct correlation between ion impact energy and local electronic temperature, justifying our fitting procedure.

Figure 13 shows the experimental data points along with model calculations for both W [Fig. 13(a)] and Fe [Fig. 13(b)]. The fitted values of z for each incident energy point are also added for reference. As the figures show, there is an excellent match between model results and the experimental data for In → W. For In → Fe, while our model predicts no kinetic emission below 7.0 keV, our results lie within tolerance of the variance of the experiment. A better fit to the In → Fe data could have been achieved lifting the $z \geq 2$ restriction, but we decided to keep the minimum number of conduction electrons to 2 for consistency with the rest of the paper. Note that a fractional z may be interpreted to represent truly mobile electrons in highly degenerate electron gases,[88] i.e., in metals, which can be significantly lower than the total number of conduction electrons. An interesting observation that emerges from this comparison exercise points to the nature of the emitted electrons. Our model separates recoil and primary emission, enabling us to quantitatively assess which mechanism is responsible for electron emission from the surface. For the results in Fig. 13, our model predicts no emission from the primary mechanism, attributing the entirety of emission to displaced recoils. In fact, the shape of the recoil contribution to IIEE, as observed in Fig. 10, closely resembles that in Fig. 13(a). In Sec. III, we discuss how emission from recoils begins at lower energies compared to emission from the primary ion in W (and most likely in other high-Z metals) while emission from the projectile starts at higher energies and is responsible for the rapid increase seen in the IIEE yields. This not only helps us to validate our model but also sheds light on the mechanism of emission in operation during experimental studies. Next, as a true validation of the fitting of z just presented, we compare our model with measurements at higher ion energies utilizing the linear dependence of z on E. For this, we compare against the results obtained by Hasselkamp *et al.*[73] for Ar → W at energies between 24 and 200 keV. Figure 14 shows the model calculations and the experimental data together, with excellent agreement found in the entire ion energy range. Note that, as discussed in Sec. IV C, there are likely morphological differences between the material surfaces in these studies that may affect the final measurements. However, those are not captured by the model at this point.

Since one of the main objectives of this body of work is to account for ion-induced electron emission from facility effects after interaction with the plume of a Hall-effect thruster at similar energies as those studied by Hugonnaud *et al.*,[83] going forward we adopt the linear relation for z observed in Fig. 13 for all subsequent simulations in the main text. It is important to note that the dependence of z on E found here represents a fitting exercise and does not provide insight into the true electronic structure of the material. These results are, thus, considered adequate validation of our model within this energy range, with the understanding that our approach does not account for crystallographic and band-structure effects.

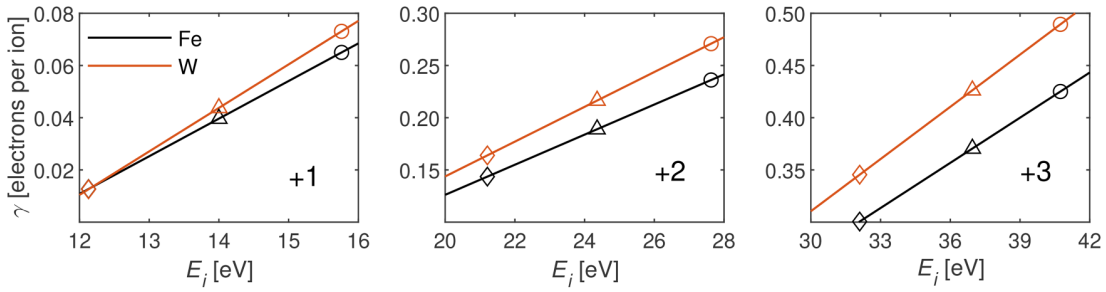

FIG. 15. Auger emission obtained from Eq. (B1) for Ar (○), Kr (△), and Xe (◇) projectiles impacting on Fe and W.

TABLE II. Ionization potentials (in eV) for singly, doubly, and triply ionized Ar, Kr, and Xe ions (from Fuggle and Mårtensson[90]).

Charge state	+1	+2	+3
Ar	15.759	27.629	40.740
Kr	13.999	24.359	36.950
Xe	12.129	21.210	32.100

APPENDIX B: EMPIRICAL ESTIMATION OF POTENTIAL ELECTRON EMISSION

A widely utilized correlation to calculate potential emission yields due to Auger neutralization is that by Kishinevsky,[89]

$$\gamma = \frac{0.2}{E_F}(0.8E_i - 2\phi), \tag{B1}$$

where E_i is the ionization potential of the incoming projectile, ϕ is the work function, and E_F is the Fermi energy of the metal. As Eq. (B1) shows, Auger neutralization in metals occurs only if the condition $(0.8E_i - 2\phi) > 0$ is met. Applying this expression to Fe and W as a function of the ionization potential of any given projectile, we generate Auger neutralization lines with specific emission points for singly, doubly, and triply ionized Ar, Kr, and Xe ions, as provided in Fig. 15. The ionization potentials for the incoming projectiles of interest are widely available and shown in Table II (from Fuggle and Mårtensson[90]). Note that this expression does not include a temperature dependence, which has been shown to be important in electron potential emission processes,[91,92] rendering it inaccurate outside of the range $3\phi < E_i < 2(E_F + \phi)$.

As the figure shows, this correlation predicts emission yields of up to 50% for multiply-charged ion states, which does not agree with experiments and represents an overestimation of potential emission yields.

REFERENCES

[1]A. Kondyurin and M. Bilek, *Ion Beam Treatment of Polymers: Application Aspects from Medicine to Space* (Newnes, 2014).
[2]A. Darafsheh, Y. Hao, X. Zhao, T. Zwart, M. Wagner, T. Evans, F. Reynoso, and T. Zhao, "Spread-out Bragg peak proton flash irradiation using a clinical synchrocyclotron: Proof of concept and ion chamber characterization," Med. Phys. **48**, 4472–4484 (2021).
[3]J. K. Hirvonen and B. D. Sartwell, *Ion Implantation* (Naval Research Laboratory, 1994).
[4]S. T. Picraux and P. S. Peercy, "Ion implantation of surfaces," Sci. Am. **252**, 102–113 (1985).
[5]J. Williams, "Ion implantation of semiconductors," Mater. Sci. Eng. A **253**, 8–15 (1998).
[6]J. Ziegler, *Handbook of Ion Implantation Technology* (Nuclear Instruments and Methods in Physics Research B, 1992).
[7]E. Ahedo, "Plasmas for space propulsion," Plasma Phys. Controlled Fusion **53**, 124037 (2011).
[8]J. Wang, D. Brinza, and M. Young, "Three-dimensional particle simulations of ion propulsion plasma environment for deep space 1," J. Spacecr. Rockets **38**, 433–440 (2001).
[9]J. M. Magnusson, A. L. Collins, and R. E. Wirz, "Polyatomic ion-induced electron emission (IIEE) in electrospray thrusters," Aerospace **7**, 153 (2020).
[10]T. Baer and R. C. Dunbar, "Ion spectroscopy: Where did it come from; where is it now; and where is it going?," J. Am. Soc. Mass Spectrom. **21**, 681–693 (2010).
[11]S. Taller, G. VanCoevering, B. D. Wirth, and G. S. Was, "Predicting structural material degradation in advanced nuclear reactors with ion irradiation," Sci. Rep. **11**, 2949 (2021).
[12]G. S. Was, "Challenges to the use of ion irradiation for emulating reactor irradiation," J. Mater. Res. **30**, 1158–1182 (2015).
[13]J. Biersack and J. Ziegler, "The stopping and range of ions in solids," in *Ion Implantation Techniques: Lectures given at the Ion Implantation School in Connection with Fourth International Conference on Ion Implantation: Equipment and Techniques Berchtesgaden, Federal Republic of Germany, 13–15 September 1982* (Springer, 1982), pp. 122–156.
[14]A. P. Horsfield, D. Bowler, H. Ness, C. Sánchez, T. N. Todorov, and A. Fisher, "The transfer of energy between electrons and ions in solids," Rep. Prog. Phys. **69**, 1195 (2006).
[15]M. Caro, A. Tamm, A. Correa, and A. Caro, "On the local density dependence of electronic stopping of ions in solids," J. Nucl. Mater. **507**, 258–266 (2018).
[16]J. Eckardt, G. Lantschner, N. Arista, and R. Baragiola, "Electronic stopping of slow molecular ions in solids," J. Phys. C: Solid State Phys. **11**, L851 (1978).
[17]D. Pines, "Electron interaction in solids," Can. J. Phys. **34**, 1379–1394 (1956).
[18]P. Nozieres and D. Pines, "Electron interaction in solids. Characteristic energy loss spectrum," Phys. Rev. **113**, 1254 (1959).
[19]A. J. Dekker, "Secondary electron emission," in *Solid State Physics* (Elsevier, 1958), Vol. 6, pp. 251–311.
[20]O. Hachenberg and W. Brauer, "Secondary electron emission from solids," in *Advances in Electronics and Electron Physics* (Elsevier, 1959), Vol. 11, pp. 413–499.
[21]W. O. Hofer, "Ion-induced electron emission from solids," Scan. Microscopy **1990**, 19 (1990).
[22]J. Sheehan, N. Hershkowitz, I. Kaganovich, H. Wang, Y. Raitses, E. Barnat, B. Weatherford, and D. Sydorenko, "Kinetic theory of plasma sheaths surrounding electron-emitting surfaces," Phys. Rev. Lett. **111**, 075002 (2013).
[23]Y. Raitses and I. D. Kaganovich, "Kinetic effects of electron-induced secondary electron emission on plasma-wall interactions," Phys. Plasmas **19**, 093511 (0000).
[24]M. Patino, Y. Raitses, and R. Wirz, "Secondary electron emission from plasma-generated nanostructured tungsten fuzz," Appl. Phys. Lett. **109**, 201602 (2016).
[25]A. Ottaviano, G. Li, C. Huerta, A. Thuppul, Z. Chen, C. Dodson, and R. Wirz, "Plasma-material interactions for electric propulsion: Challenges, approaches and future," in *The 36th International Electric Propulsion Conference, Austria* (Electric Rocket Propulsion Society, 2019).
[26]H.-Y. Chang, A. Alvarado, and J. Marian, "Calculation of secondary electron emission yields from low-energy electron deposition in tungsten surfaces," Appl. Surf. Sci. **450**, 190–199 (2018).
[27]H.-Y. Chang, A. Alvarado, T. Weber, and J. Marian, "Monte Carlo modeling of low-energy electron-induced secondary electron emission yields in micro-architected boron nitride surfaces," Nucl. Instrum. Methods Phys. Res. Sec. B **454**, 14–22 (2019).
[28]A. Alvarado, H.-Y. Chang, W. Nadvornick, N. Ghoniem, and J. Marian, "Monte Carlo raytracing method for calculating secondary electron emission from micro-architected surfaces," Appl. Surf. Sci. **478**, 142–149 (2019).
[29]K. Ohya, "Monte Carlo simulation of heavy ion induced kinetic electron emission from an al surface," Nucl. Instrum. Methods Phys. Res. Sec. B **195**, 281–290 (2002).
[30]C. E. Huerta and R. E. Wirz, "Ion-induced electron emission reduction via complex surface trapping," AIP Adv. **9**, 125009 (2019).
[31]E. Sternglass, "Theory of secondary electron emission by high-speed ions," Phys. Rev. **108**, 1 (1957).
[32]R. Baragiola, E. Alonso, J. Ferron, and A. Oliva-FIorio, "Ion-induced electron emission from clean metals," Surf. Sci. V **90**, 1979 (1979).
[33]J. Schou, "Transport theory for kinetic emission of secondary electrons from solids," Phys. Rev. B **22**, 2141 (1980).
[34]R. A. Baragiola, "Principles and applications of ion-induced Auger electron emission from solids," Radiat. Effects **61**, 47–72 (1982).
[35]A. Schleife, Y. Kanai, and A. A. Correa, "Accurate atomistic first-principles calculations of electronic stopping," Phys. Rev. B **91**, 014306 (2015).
[36]A. A. Correa, "Calculating electronic stopping power in materials from first principles," Comput. Mater. Sci. **150**, 291–303 (2018).
[37]R. Ullah, E. Artacho, and A. A. Correa, "Core electrons in the electronic stopping of heavy ions," Phys. Rev. Lett. **121**, 116401 (2018).

[38]D. Pines, "A collective description of electron interactions: IV. Electron interaction in metals," Phys. Rev. **92**, 626 (1953).
[39]J. Bardeen and D. Pines, "Electron-phonon interaction in metals," Phys. Rev. **99**, 1140 (1955).
[40]D. Van der Marel and G. Sawatzky, "Electron-electron interaction and localization in *d* and *f* transition metals," Phys. Rev. B **37**, 10674 (1988).
[41]G. F. Dionne, "Origin of secondary-electron-emission yield-curve parameters," J. Appl. Phys. **46**, 3347–3351 (1975).
[42]K. I. Grais and A. Bastawros, "A study of secondary electron emission in insulators and semiconductors," J. Appl. Phys. **53**, 5239–5242 (1982).
[43]F. Gebhard and F. Gebhard, *Metal–Insulator Transitions* (Springer, 1997).
[44]K. Kanaya, S. Ono, and F. Ishigaki, "Secondary electron emission from insulators," J. Phys. D: Appl. Phys. **11**, 2425 (1978).
[45]S. Tougaard, "Universality classes of inelastic electron scattering cross-sections," Surf. Interface Anal. **25**, 137–154 (1997).
[46]R. Baragiola and P. Riccardi, "Electron emission from surfaces induced by slow ions and atoms," in *Reactive Sputter Deposition* (Springer, 2008), pp. 43–60.
[47]R. Baragiola, E. Alonso, and H. Raiti, "Ion-induced Auger-electron emission from aluminum," Phys. Rev. A **25**, 1969 (1982).
[48]T. Åberg, "Unified theory of Auger electron emission," Phys. Scr. **1992**, 71 (1992).
[49]G. A. Harrower, "Auger electron emission in the energy spectra of secondary electrons from Mo and W," Phys. Rev. **102**, 340 (1956).
[50]R. Beuhler and L. Friedman, "Low noise, high voltage secondary emission ion detector for polyatomic ions," Int. J. Mass Spectrom. Ion Phys. **23**, 81–97 (1977).
[51]R. Beuhler and L. Friedman, "Larger cluster ion impact phenomena," Chem. Rev. **86**, 521–537 (1986).
[52]D. Hasselkamp, H. Rothard, K.-O. Groeneveld, J. Kemmler, P. Varga, and H. Winter, *Particle Induced Electron Emission II* (Springer, 2006), Vol. 123.
[53]L. Yang, B. Da, H. Yoshikawa, S. Tanuma, J. Hu, J. Liu, D. Tang, and Z. Ding, "Low-energy electron inelastic mean free path and elastic mean free path of graphene," Appl. Phys. Lett. **118**, 053104 (2021).
[54]K. Krebs, "Recent advances in the field of ion-induced kinetic electron emission from solids," Vacuum **33**, 555–563 (1983).
[55]J. F. Ziegler, J. P. Biersack, and U. Littmark, *The Stopping and Range of Ions in Matter* (Pergamon Press, New York, 1985).
[56]J. F. Ziegler, M. Ziegler, and J. Biersack, "SRIM—The stopping and range of ions in matter (2010)," Nucl. Instrum. Methods Phys. Res Sec. B **268**, 1818–1823 (2010).
[57]See https://www-nds.iaea.org/stopping/stopping_201410/SCSLists/tables.txt for information about stopping tables.
[58]D. K. Brice, "Three-parameter formula for the electronic stopping cross section at nonrelativistic velocities," Phys. Rev. A **6**, 1791 (1972).
[59]E. Artacho, "Electronic stopping in insulators: A simple model," J. Phys.: Condens. Matter **19**, 275211 (2007).
[60]R. Lipperheide, T. Weis, and U. Wille, "Generalized drude model: Unification of ballistic and diffusive electron transport," J. Phys.: Condens. Matter **13**, 3347 (2001).
[61]K. L. Jensen, *Introduction to the Physics of Electron Emission* (John Wiley & Sons, 2017).
[62]D. Rai and R. Thapa, "A theoretical study of bulk tungsten (W) based on momentum transfer (-dependent)," Adv. Opt. **2014**, 814909 (2014).
[63]M. Häfner, J. K. Viljas, D. Frustaglia, F. Pauly, M. Dreher, P. Nielaba, and J. C. Cuevas, "Theoretical study of the conductance of ferromagnetic atomic-sized contacts," Phys. Rev. B **77**, 104409 (2008).
[64]F.-Y. Lo, "Magnetotransport in cleaved-edge-overgrown Fe/GaAs-based and rare-earth-doped GaN-based heterostructures" Thesis/Dissertation. Report Number: ETDE-DE-1701 (Research Organizations:Bochum Univ. 2007).
[65]F. Marlow, S. Josten, and S. Leiting, "Electronics with stainless steel: The work functions," J. Appl. Phys. **133**, 085104 (2023).
[66]N. W. Ashcroft and N. D. Mermin, *Solid State Physics* (Cengage Learning, 2022).
[67]B. Hopkins and J. Rivière, "The work function of polycrystalline tungsten foil," Proc. Phys. Soc. **81**, 590 (1963).
[68]C. Lemell, B. Solleder, K. Tőkési, and J. Burgdörfer, "Simulation of attosecond streaking of electrons emitted from a tungsten surface," Phys. Rev. A **79**, 062901 (2009).
[69]J. Mischler and N. Benazeth, "Ion-induced auger emission from solid targets," Scan. Electron Microsc. **1986**, 3 (1986).
[70]E. Alonso, R. Baragiola, J. Ferron, M. Jakas, and A. Oliva-Florio, "Z_1 dependence of ion-induced electron emission from aluminum," Phys. Rev. B **22**, 80 (1980).
[71]N. Bajales, S. Montoro, E. Goldberg, R. Baragiola, and J. Ferrón, "Identification of mechanisms of ion induced electron emission by factor analysis," Surf. Sci. **579**, 97–102 (2005).
[72]G. Kowarik, M. Brunmayr, and F. Aumayr, "Electron emission from tungsten induced by slow, fusion-relevant ions," Nucl. Instrum. Methods Phys. Res. Sec. B **267**, 2634–2637 (2009).
[73]D. Hasselkamp, K. Lang, A. Scharmann, and N. Stiller, "Ion induced electron emission from metal surfaces," Nucl. Instrum. Methods **180**, 349–356 (1981).
[74]Y. Yamamura, "A simple analysis of the angular dependence of light-ion sputtering," Nucl. Instrum. Methods Phys. Res. Sec. B **2**, 578–582 (1984).
[75]S. Walton, J. Tucek, R. Champion, and Y. Wang, "Low energy, ion-induced electron and ion emission from stainless steel: The effect of oxygen coverage and the implications for discharge modeling," J. Appl. Phys. **85**, 1832–1837 (1999).
[76]M. Thompson, "The velocity distribution of sputtered atoms," Nucl. Instrum. Methods Phys. Res. Sec. B **18**, 411–429 (1986).
[77]J. Marian, L. A. Zepeda-Ruiz, N. Couto, E. M. Bringa, G. H. Gilmer, P. C. Stangeby, and T. D. Rognlien, "Characterization of sputtering products during graphite exposure to deuterium ions by molecular dynamics," J. Appl. Phys. **101**, 044506 (2007).
[78]M. Kaminsky, *Atomic and Ionic Impact Phenomena on Metal Surfaces* (Springer Science & Business Media, 2013), Vol. 25.
[79]V. Popok and E. E. Campbell, "Beams of atomic clusters: Effects on impact with solids," Rev. Adv. Mater. Sci. **11**, 19–45 (2006).
[80]R. D. Bland, G. Kominiak, and D. Mattox, "Effect of ion bombardment during deposition on thick metal and ceramic deposits," J. Vac. Sci. Technol. **11**, 671–674 (1974).
[81]S. G. Mayr and R. Averback, "Effect of ion bombardment on stress in thin metal films," Phys. Rev. B **68**, 214105 (2003).
[82]D. M. Mattox and G. Kominiak, "Structure modification by ion bombardment during deposition," J. Vac. Sci. Technol. **9**, 528–532 (1972).
[83]V. Hugonnaud, S. Mazouffre, and D. Krejci, "Ion-induced electron emission by keV-range energy indium ions: Influence of material and geometry," J. Appl. Phys. **132**, 193302 (2022).
[84]D. Krejci, A. Reissner, T. Schönherr, B. Seifert, Z. Saleem, and R. Alejos, "Recent flight data from IFM Nano Thrusters in a low earth orbit," in *36th International Electric Propulsion Conference* (Electric Rocket Propulsion Society, 2019), pp. 15–20.
[85]T. Schönherr, B. Little, D. Krejci, A. Reissner, and B. Seifert, "Development, production, and testing of the IFM Nano FEEP Thruster," in *36th International Electric Propulsion Conference* (Electric Rocket Propulsion Society, 2019), pp. 1–11.
[86]A. Duvenbeck, B. Weidtmann, and A. Wucher, "Predicting kinetic electron emission in molecular dynamics simulations of sputtering," J. Phys. Chem. C **114**, 5715–5720 (2010).
[87]E. Bévillon, J.-P. Colombier, V. Recoules, and R. Stoian, "Free-electron properties of metals under ultrafast laser-induced electron-phonon nonequilibrium: A first-principles study," Phys. Rev. B **89**, 115117 (2014).
[88]V. Palenskis, "The effective density of randomly moving electrons and related characteristics of materials with degenerate electron gas," AIP Adv. **4**, 047119 (2014).
[89]L. Kishinevsky, "Estimation of electron potential emission yield dependence on metal and ion parameters," Radiat. Effects **19**, 23–27 (1973).
[90]J. C. Fuggle and N. Mårtensson, "Core-level binding energies in metals," J. Electron. Spectrosc. Relat. Phenom. **21**, 275–281 (1980).
[91]S. Valeri, "Auger electron emission by ion impact on solid surfaces," Surf. Sci. Rep. **17**, 85–150 (1993).
[92]C. Benazeth, P. Hecquet, C. Mayoral, and N. Benazeth, "Temperature dependence of ion-induced auger electron emission from (111) silicon: I. Experiments," Radiat. Effects Defects Solids **108**, 227–239 (1989).